# A Level-Set Method for Simulation of Drop Motions

Gihun Son, Nahmkeon Hur, Youngho Suh, and Sanghyuk Lee

Department of Mechanical Engineering, Sogang University, Seoul, Korea
(Tel : +82-2-705-8641; E-mail: gihun@sogang.ac.kr, nhur@sogang.ac.kr)

**Abstract**: A level-set method is developed for computation of drop motions in various engineering applications. Compared with the volume-of-fluid method based on a non-smooth volume-fraction function, the LS method can calculate an interface curvature more accurately by using a smooth distance function. Also, it is straightforward to implement for two-phase flows in complex geometries unlike the VOF method requiring much more complicated geometric calculations. The LS method is applied to simulation of inkjet process, thin film pattering and droplet collisions.

**Keywords:** A level-set method, Two-phase flow, Inkjet, Thin film pattering , Droplet collision

## 1. INTRODUCTION

The volume-of-fluid (VOF) method where the interface is tracked by the VOF function representing the volume fraction of a particular phase in each cell, has been widely used for computing two-phase flows with topologically complex interfaces. While discretizing the advection equation of the volume fraction, whose spatial derivatives are not continuous, the VOF method requires a special calculation procedure based on the interface configurations which are determined (or reconstructed) from the VOF function. The method has been improved employing a piecewise linear interface calculation (PLIC) method, in which the advected fractional volume is evaluated geometrically from the reconstructed interface. Generally, the PLIC VOF method preserves volume conservation very well, but its implementation for two-phase flows in irregular geometries requires very complicated geometric calculations for the interface reconstruction, and the discretization of the interface curvature is not straightforward. As another Eulerian method, a level-set (LS) method was developed by Sussman et al. [1] for incompressible two-phase flows with large density ratios. In the method, the interface is tracked by the LS function defined as a signed distance from the interface. As a smooth and continuous function, the LS function can calculate the interface curvature accurately.

The LS formulation is extended to simulate a inkjet process, in which liquid is ejected through a micro nozzle by a pressure pulse that results from the movement of a piezoelectric element. Inkjet printing technology has recently received increasing attention in various patterning processes such as required in manufacturing color filters of LCD, DNA micro array, organic TFT devices, light-emitting diodes, and micro-lens. Significant efforts have been made to develop a numerical method for analysis of the inkjet process which can be used to find the optimal design parameters in various inkjet applications. The VOF method has been widely used for computing the retraction and ejection of liquid jet through a nozzle[2-3]. The method has been improved by employing a geometric calculation procedure known as a PLIC algorithm. However, it is not simple to implement the geometric condition for a contact angle, which is formed at the liquid-gas-solid contact line. The implementation is much more complicated for a real surface with contact angle hysteresis where the contact angle varies dynamically between advancing and receding contact angles. Also, the PLIC VOF method is not straightforward to implement for multiphase flows including an immersed solid surface with contact angle hysteresis because it requires quite complicated geometric calculations to reconstruct the interface configuration satisfying the contact angle condition as well as the volume fraction in an irregular fluid region. Very recently, Yu et al.[4] have developed the LS method for simulation of droplet ejection in inkjet printing. Since the LS function is smooth and continuous, the interface determination is much simpler than in the VOF method requiring geometric calculations. Yu et al. included a dynamic contact angle model in the LS formulation. In their computation, however, the nozzle shape was relatively simple so that the contact angle condition could be applied without systematic implementation procedures.

In this study, we propose the LS method which can treat the contact angle condition at an immersed solid surface for computation of droplet ejection and droplet deposition on the pre-patterned micro-structure in inkjet printing process. Also, the LS method is further extended for two-phase flows on non-orthogonal grids. The method is applied to simulation of drop collision and drop impact on a liquid film or pool.

## 2. NUMERICAL FORMULATION

### 2.1 Governing equations

The interface separating the two phases is tracked by a LS function, $\phi$, which is defined as a signed distance from the interface. The negative sign is chosen for the gas phase and the positive sign for the liquid phase. The continuity and momentum equations for the gas-liquid region are written as

$$\nabla \cdot \vec{u} = 0 \tag{1}$$

$$\rho \frac{\partial \vec{u}}{\partial t} = -\nabla p + \nabla \cdot \mu \nabla \vec{u} + \vec{f} \tag{2}$$

where,

$$\vec{f} = -\rho \vec{u} \cdot \nabla \vec{u} + \rho \vec{g} - \sigma \kappa \nabla H_\phi + \nabla \cdot \mu \, (\nabla \vec{u})^T$$

$$H_\phi = 0 \quad \text{if } \phi \le 0$$

$$= 1 \quad \text{if } \phi > 0$$

$$\rho = \rho_g (1 - H_\phi) + \rho_l H_\phi; \quad \mu = \mu_g (1 - H_\phi) + \mu_l H_\phi$$

$$\kappa = \nabla \cdot (\nabla \phi / |\nabla \phi|)$$

In the LS formulation, the interface is described as $\phi = 0$. The zero level set of $\phi$ is advanced by the fluid velocity while solving the equation

$$\frac{\partial \phi}{\partial t} + \vec{u} \cdot \nabla \phi = 0 \tag{3}$$

The LS function is reinitialized to a distance function ($|\nabla \phi| = 1$) from the interface by obtaining a steady-state

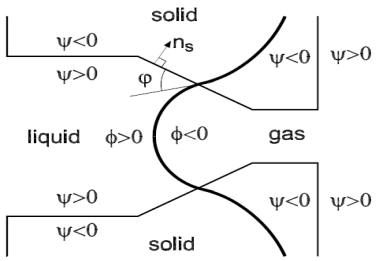


Fig. 1 Definitions of level-set functions ( $\phi$ , $\psi$ ) and contact angle ( $\varphi$ ).

solution of the equation

$$\frac{\partial \phi}{\partial \tau} = S(1 - |\nabla \phi|) \tag{4}$$

$$S = 0 \qquad \text{if } |\phi| \le h/2$$

$$= \frac{\phi}{\sqrt{\phi + h^2}} \qquad \text{otherwise} \tag{5}$$

Here, $h$ is a grid spacing and S is smoothed sign function.

**2.2 Modification for immersed solid surfaces**

To treat the immersed solid surfaces, we introduce another level set function, $\psi$ , which is defined as a signed distance from the fluid-solid interface. The negative sign is chosen for the solid region and the positive sign for the fluid region. Assuming that the solid is stationary, the continuity and momentum equations for $H_\psi = 1$ described previously can be extended for two-fluid flows with immersed solid surfaces as

$$\nabla \cdot \vec{u} = 0 \tag{6}$$

$$\rho \frac{\partial \vec{u}}{\partial t} = -H_\psi \nabla p + \nabla \cdot \mu_e \nabla \vec{u} + H_\psi \vec{f} \quad \text{if } H_\psi > 0$$
$$\vec{u} = 0 \quad \text{if } H_\psi = 0 \tag{7}$$

where $\mu_e$ is an effective viscosity defined as $\mu / H_\psi$ . The effective viscosity formulation helps to get a correct viscous stress near the immersed solid boundary.

To implement the contact angle condition at the liquid-gas-solid contact line, the LS advection equation is modified as

$$\frac{\partial \phi}{\partial t} + \vec{u} \cdot \nabla \phi = 0 \qquad \text{if} \quad \psi > 0 \tag{8}$$

$$n_s \cdot \nabla \phi = \cos \varphi \qquad \text{if} \quad \psi = 0 \tag{9}$$

The unit normal vector $n_s$ pointing into the solid region and the contact angle $\varphi$ is defined as shown in Fig. 1. In Eq. (9) the contact angle condition defined at the liquid-gas-solid contact line is extended into the entire solid region in which the level-set function for liquid-gas phases is not well defined; otherwise the zero level set of $\phi$ will have a steep variation near the fluid-solid interface. For numerical implementation, Eq. (9) is replaced by the iterative equation

$$\frac{\partial \phi}{\partial \tau} = \cos \varphi - n_s \cdot \nabla \phi \tag{10}$$

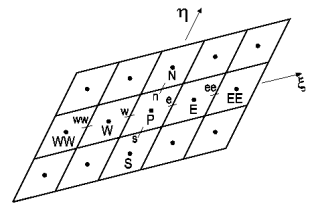


Fig. 2 Control volume

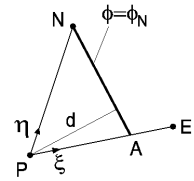


Fig. 3 Schematic for 2-D discretization of $|\nabla \phi|$

**2.3 Extension for non-orthogonal grid**

The LS formulation is further extended for drop motion on non-orthogonal grid. The continuity and momentum equations are solved by following the calculation procedure proposed by Peric[5] for single-phase flows in general coordinates. Cartesian velocity components are used as dependent variables in the momentum equations, which results in much simpler equations than covariant or contravariant velocity components. Also, we adopt a non-staggered grid system in which all the flow properties are defined at cell centers. A pressure-velocity decoupling problem, which possibly happens using the non-staggered grid system without special care, is resolved by an interpolation technique for appropriate valuation of the pressure gradients at cell faces while discretizing the continuity equation. Since the discretization and solution procedures for the continuity and momentum equations are described in detail by the references, we focus only on the discretization of the LS equations.

The LS advection Eq. (3) is discretized for grid point P shown in Fig. 2 as

$$\frac{(\phi_p^{n+1} - \phi_p^n)}{\Delta t} + F_e \phi_e^n - F_w \phi_w^n + F_n \phi_n^n - F_s \phi_s^n = 0 \tag{11}$$

Here F's are the volumetric flow rates through the faces of the control volume, and $\phi$ 's at the cell faces are evaluated by using a second-order essentially non-oscillatory (ENO) scheme.

The LS reinitialization Eq. (4) is discretized to reconstruct the LS function to a signed distance function by upwinding away from the interface. $|\nabla \phi|$ can be easily formulated if employing only a coordinate transformation technique as applied to the continuity and momentum equations, but the formulation without geometric constraints caused by the non-orthogonality of grids produces additional errors. In this article, we present a calculation procedure for $|\nabla \phi|$ with the geometric constraints. If rotating each computational cell so that $|\phi_\xi| \ge |\phi_\eta|$ , we can consider the case depicted in Fig. 3. The calculation procedure for $|\nabla \phi|$ is summarized as follows:

1. If $|\phi_\xi| = 0$ , $|\nabla \phi| = 0$ . This means the LS function should not be reinitialized by using the points further away from the interface.

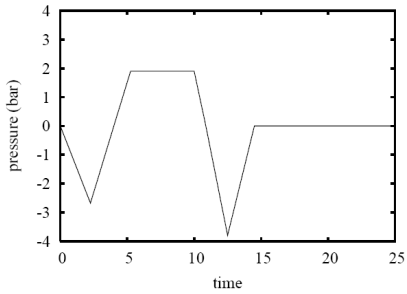


Fig. 4 Temporal variation of imposed inflow pressure.

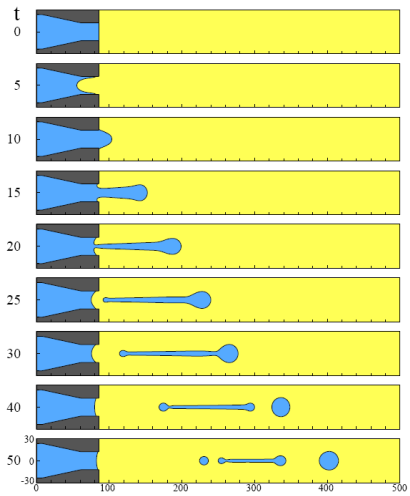


Fig. 5 Droplet motion in an inkjet process.

2. If $|\phi_\xi| > 0$ and $|\phi_\eta| = 0$, $|\nabla\phi| = |\phi_\xi|$.

3. If $|\phi_\eta| > 0$, $|\nabla\phi| = |\phi_\eta| d_{PN} / d_{\min}$.

Here $d_{\min}$ is the shortest distance between point P and line segment AN as shown in Fig. 3, and point A is determined from the interpolation $d_{AP} = d_{NP} |\phi_\eta| / |\phi_\xi|$. Introducing a parameter s, the distance between point P and line segment AN is expressed as

$$Q(s) = |\vec{d}_{AP} + s(\vec{d}_{NP} - \vec{d}_{AP})| \quad (12)$$

$$Q(s) = (a_2 s^2 + 2a_1 s + d_{AP}^2)^{1/2} \quad (13)$$

where Q has a minimum value when $s_o = -a_1 / a_2$. It is noted that $s_o < 1/2$ since $|\phi_\xi| \geq |\phi_\eta|$. If $s_o < 0$, which doest not occur when using orthogonal grids, the projection of point P onto the line can lie off the segment AN and then $d_{\min} = Q(0)$. Considering the geometric constraint caused by the non-orthogonality of grids, the shortest distance is expressed as $d_{\min} = Q[\max(s_o, 0)]$. This calculation procedure for $|\nabla\phi|$ can be extended for three-dimensional case.

## 3. RESULT AND DISCUSSION

### 3.1 Drop motion in inkjet

The computations are performed for a piezoelectric inkjet, which is described in axisymmetric coordinates. Based on

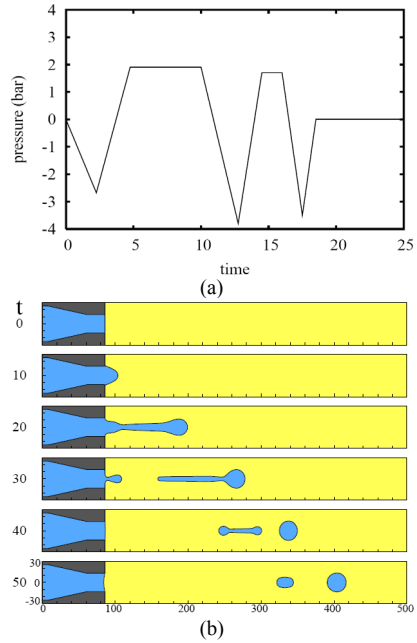


Fig. 6 An inkjet process with double pressure pulse: (a) the imposed inflow pressure and (b) the computed droplet motion.

the work of Yu et al.[4], we use a nozzle diameter of 25 $\mu m$, the advancing contact angles of $\varphi_a$ =70°, receding contact angles of $\varphi_r$ =20° and the ink properties. Fig. 4 depicts the pressure pulse imposed at the nozzle bottom.

Fig. 5 shows the droplet motion and the associated velocity field in a piezoelectric inkjet process. During the early period, the liquid is retracted into the nozzle by a negative pressure pulse. Thereafter, while the pressure forcing is positive, the liquid is ejected through a nozzle and forms an elongated column. It is seen at t = 15 $\mu s$ that the liquid inside the nozzle is pulled back by the second negative pressure pulse while the ejected liquid column is moving forward. As the liquid column becomes thinner at the nozzle exit, it pinches off near t = 20 $\mu s$. Thereafter the liquid column breaks into one primary droplet and then multiple satellite droplets. The volumes of the primary droplet and the multiple satellite droplets are 8.24pl and 3.08pl, respectively. The remaining liquid inside the nozzle forms a concave meniscus, which derives the liquid to be refilled into the nozzle, as shown during the period of $25\mu s \leq t \leq 50\mu s$. The droplet ejection pattern is comparable to the numerical results and experimental imgaes reported in the literature Yu et al.[4].

In a piezoelectric inkjet process, the formation of satellite droplets is undesirable in high quality printing. As one of the methods to reduce the volume of satellite droplets, a double-peak type of pressure pulse has recently been proposed in the literature [6]. Its feasibility is tested through the numerical simulation with the pressure pulse modified as in Fig. 6(a). A short pressure pulse is added to the original pressure pulse. Figure 14b shows the computed droplet motion. A short positive and negative pressure pulse is added at t=15 $\mu s$, when the ejected liquid column starts to pinch off at the nozzle exit. The additional pressure pulse pushes out and pulls back the liquid column. This causes the pinch-off location of liquid column to shift toward the head of the

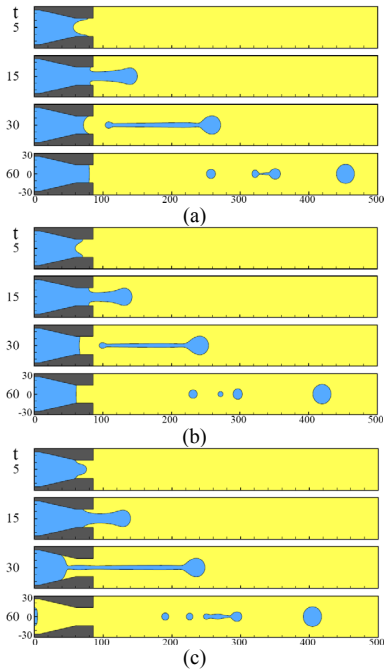


Fig. 7 Effect of receding contact angle on droplet ejection at $\varphi_a$ =150°: (a) $\varphi_r$ = 30°, (b) $\varphi_r$ = 90°, and (c) $\varphi_r$ = 150°.

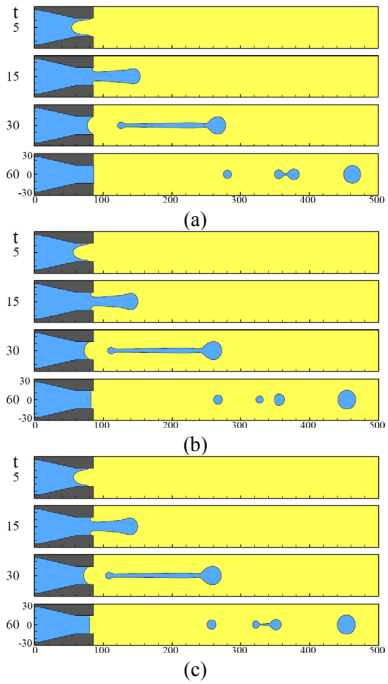


Fig. 8 Effect of receding contact angle on droplet ejection at $\varphi_r$ = 30°: (a) $\varphi_a$ = 30°, (b) $\varphi_a$ = 90°, and (c) $\varphi_a$ = 150°.

column. In other words, the pinched-off liquid column becomes shorter due to the additional pressure pulse. As a result, the volume of satellite droplets is reduced by up to 32% without losing the speed of the primary droplet.

Fig. 7 presents the effect of receding contact angle on the droplet ejection pattern while keeping $\varphi_a$ =150°. It is seen at t=5 $\mu s$ that as the receding contact angle increases, the liquid-gas-solid contact point is more easily retracted into the nozzle by a negative pressure pulse. The liquid-gas interface is deformed to satisfy the contact angle condition at the nozzle wall. The difference in interface deformation is somewhat reduced during the liquid ejection period when the imposed positive pressure force is dominant over the surface tension force. However, while the liquid is retracted again into the nozzle by the second negative pressure pulse and the ejected liquid column pinches off for t>15 $\mu s$ , the effect of receding contact angle on the interfacial motion is pronounced inside the nozzle. For $\varphi_a \geq 90^o$ , the interface does not form a concave meniscus and thus the liquid refill process is not observed in the nozzle. This demonstrates that in designing an inkjet printhead, it is desirable to keep the receding contact angle smaller than 90°. The effect of advancing contact angle on the droplet motion at $\varphi_r$ =30° is plotted in Fig. 8. It is observed that the variation of advancing contact angle has little influence on the whole droplet ejection process. However, for $30\mu s \leq t \leq 50\mu s$ , the ink refill rate decreases slightly as the advancing contact angle increases. This is caused by the fact that the axial component of surface tension force, which pulls up the interface, decreases with the advancing contact angle.

### 3.2 Drop motion in film patterning

For high resolution patterning, it is very important to accurately place a droplet to the target position. However, the

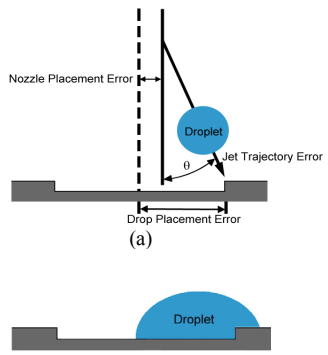


Fig. 9 Schematic diagram of inkjet patterning process: (a) droplet placement error and (b) undesired droplet deposition.

inkjet process possibly has some undesired patterning errors caused by the inaccuracy in nozzle position and ejecting angle, as shown in Fig. 9. One of the efficient techniques to overcome the patterning error is to use the multiphase characteristics between the liquid-gas-solid phases. An example is to self-align a droplet on the combination of hydrophilic substrate and hydrophobic micro-structure by controlling the surface energy at the contact of three phases [7].

In this study, we performed a numerical simulation of micro droplet deposition on the pre-patterned micro-structure. Fig. 10 shows the numerical results of droplet deposition pattern with droplet placement error. In the computation, the droplet has a diameter of 35 $\mu m$ , the hole has a width of 50 $\mu m$ and a depth of 10 $\mu m$ . The impact velocity of droplet is

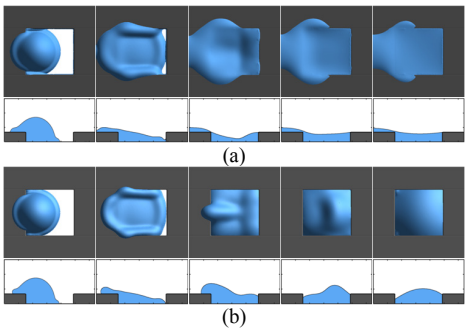

Fig. 10 Effect of contact angle of cavity wall on droplet motion with droplet placement error: (a) $\varphi_{structure}$ =30°, $\varphi_{substrate}$ =30° and (b) $\varphi_{structure}$ =30°, $\varphi_{substrate}$ =120°.

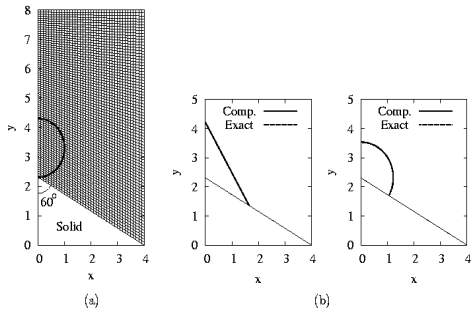


Fig. 11 Droplet motion on an inclined wall under no gravity condition: (a) an initial interface on non-orthogonal meshes and (b) the steady droplet shapes at $\varphi_r = \varphi_a = 30^o$ and $\varphi_r = \varphi_a = 90^o$

8m/s and the substrate has a contact angle of 30°. In the case of $\varphi_{structure}$ =30°, the droplet spreads on both of the micro-structure and substrate and some portion of ink is left on microstructure. In contrast, when the contact angle of micro-structure is increased to 120°, most of droplet is observed to fill the hole. The numerical simulation of a patterning process using microdroplet ejection demonstrates that the multiphase characteristics between the liquid-gas solid phases can be used to overcome the patterning error.

### 3.3 Drop motion on an inclined wall

To validate the LS formulation on non-orthogonal grid, the drop motion on an inclined wall was also analyzed. The computational grids and initial conditions for a drop motion on the inclined wall are shown in Fig. 11(a). All boundaries of the domain are specified by the no-slip and contact angle condition. A semicircular drop is initially placed on the left side wall with no gravity force. And the non-dimensional parameters are $\rho_l/\rho_g = 1000$, $\mu_l/\mu_g = 100$, Re (= $\rho_l UD/\mu_l$)=44.7 and We(= $\rho_l U^2 D/\sigma$)=1. From this simulation, Fig. 11(b) shows the numerical results with the contact angle of $\varphi_a = \varphi_r = 30°$ and $\varphi_a = \varphi_r = 90°$. The steady-state drop shape is formed by the shape of a straight line or a truncated circle that satisfied a specified contact angle. And the numerical results at the steady state have no differences with the exact solution. Also, the drop motions with gravity force are shown in Fig. 12. In these cases, the gravitational force is dominant over the surface tension force holding the drop on the left side wall and hence the drop slides

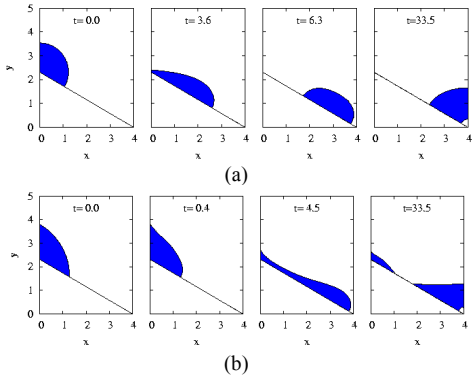


Fig 12. Droplet motion on an inclined wall for (a) $\varphi_r = \varphi_a = 90^o$ and Fr=1 and (b) $\varphi_a = 90^o$, $\varphi_r = 30^o$ and Fr=0.5

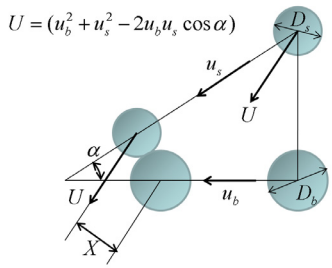


Fig. 13 Schematic of binary drop collision

down an inclined wall. Then, the drop behavior is determined by the contact angle condition.

### 3.4 Binary drop collision

In this study, the binary drop collision was numerically simulated by using LS method. When the drop collision occurs, the interactions of drops are influenced by the drop property, drop velocity, drop-size and impact parameter. These parameters can be summarized by the non-dimensional parameter; Weber number, Ohnesorge number, drop-size ratio ( $\Delta = D_s/D_b$ ) and non-dimensional impact parameter ( $x = 2X/(D_b + D_s)$ ). By the effects of these parameters, the collision processes are generated with the complicated phenomena. The drop collision can be classified into four interactions such as the bouncing, coalescence, reflexive separation and stretching separation. The bouncing regime is observed in the hydrocarbon drop collision. When the bouncing occurs, the gas layer around the drop disturbed the coalescence of two drops. However, this phenomenon cannot be shown in case of water drop coalescence. In this study, the simulations on the regimes of the coalescence, reflexive separation and stretching separation were performed.

Fig. 13 shows the schematic of binary drop collision. The simulations on the drop collision were analyzed with two different conditions of head-on and off-center collision. 2D axisymmetric simulation on head-on collisions and 3D simulation on off-center collision were performed. From these simulations, the behavior of drops and formation of satellite drop were obtained. Fig. 14 shows the results of the head-on collision with various conditions. As Weber number increases, the reflexive energy increases. Therefore, the reflexive separation occurs easily with high Weber number. And the size of satellite drop increases. Then, the secondary satellite

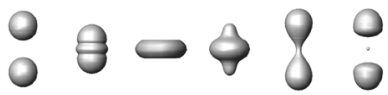

(a) We=23 and Δ =1.0

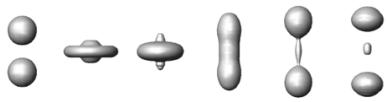

(b) We=40 and Δ =1.0

(c) We=56 and Δ =0.5

Fig. 14 Drop behavior of head-on collision

(a) We=83, Δ =1.0 and x=0.34

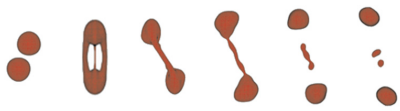

(b) We=83, Δ =1.0 and x=0.43

Fig. 15 Drop behavior of off-center collision

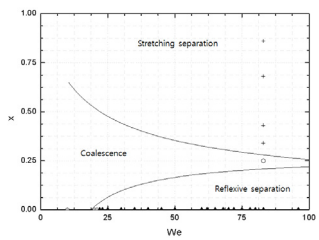


(a)

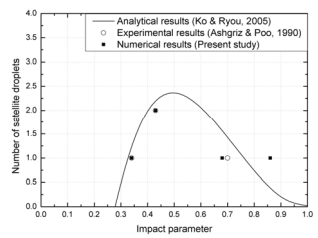


(b)

Fig. 16 Comparison of numerical results with experimental and theoretical results: (a) Interaction regimes of drop collision and (b) Number of satellite drop.

drops may be separated from the bigger satellite drop. Fig. 15 shows the results of the off-center collision with various conditions. In the low impact parameter, the reflexive separation is generated like in Fig. 14. As the impact parameter increases, the stretching energy becomes bigger. When the stretching energy is similar to the reflexive energy,

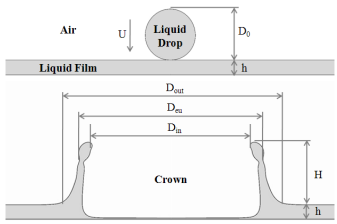


Fig. 17 Schematic of the drop impact on liquid film

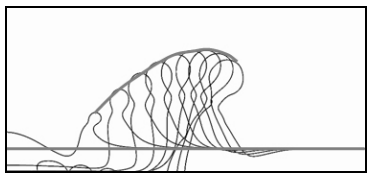

Fig. 18 Drop splashing and spreading (We=297, $\delta$ =0.29)

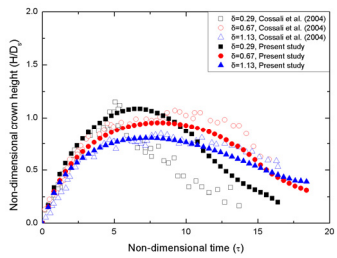


(a)

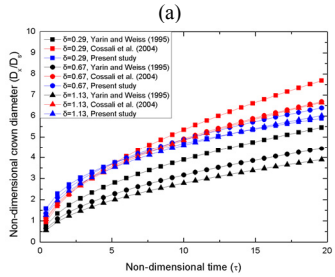


(b)

Fig. 19 Characteristics of the crown with various film thickness (We=297): (a) Crown heights and (b) Crown diameters.

the coalescence of two drops occurs. And then, the stretching separation is generated in the high impact parameter. From these results, the characteristics of drop collision compared with the experimental data[8] and theoretical results[9] like in Fig. 16. The interaction regimes of drop collision with various Weber number and impact parameters are shown in Fig. 16(a) and the numbers of satellite drops with various impact parameters are shown in Fig. 16(b). These numerical results have a good agreement with the previous correlations.

### 3.4 Drop impact on a liquid film

When the drop impacts on the surface, the phenomenon of drop impact is determined by the property of the surface such as a dry and wetted surface and liquid pool. In this chapter, the drop impact on the liquid film was numerically analyzed. The phenomenon of drop impact on liquid film depends on the drop property, impact velocity, drop size and liquid film thickness. These parameters can be summarized by the two main non-dimensional parameter; Weber number and non-

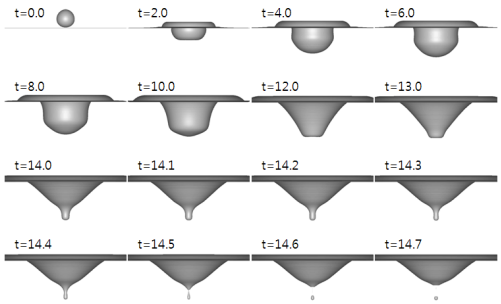


Fig. 20 Bubble entrapment (Fr=200, We=138, H=4D)

dimensional film thickness ( $\delta = h / D_0$ ). By the effects of these parameters, the splashing and the crown formation and propagation are generated. In this study, 2D axisymmetric simulations of the drop splashing and spreading due to the water drop impact on liquid film were analyzed with Weber number of 297.

Fig. 17 shows the schematic of the drop impact on liquid film. A spherical drop with velocity U impacts on the liquid film with thickness h. Since the kinetic energy of the impacting drop is reflected by the static liquid film, the crown forms in the contact area between drop and liquid film. After a drop impacts on liquid film, the drop splashing and spreading are generated like Fig. 18. The crown height grows up and the secondary drop may be generated by the flow instability. After crown height reaches maximum value, the crown height is decreased by the gravity. Fig. 19(a) shows the evolution of the crown height with various film thicknesses. This numerical result of crown height has a good agreement with the experimental results of Cossali et al.[10]. After a drop impacts on the liquid film, the crown spreads outward. Fig. 19(b) shows the evolution of the crown diameter defined by the outer diameter of the neck below the crown rim. These numerical results compared with previous empirical correlation[10,11]. The correlation of Yarin and Weiss[11] underestimates the crown diameter than Cossali et al.[10] because Yarin and Weiss[11] do not consider film thickness. The numerical results of the present study corresponded with Cossali et al.[10]

### 3.5 Drop impact on a liquid pool

In this study, the formation of bubble due to initial drop impact was numerically analyzed. When a spherical drop impacts on the liquid pool, the bubble can be generated by cavity collapse. This drop entrapment is influenced by the drop property, impact velocity and gravity force. These parameters can be summarized by two non-dimensional parameter; Weber number and Froude number( $Fr = U^2 / gD$ ). In the present study, 2D axisymmetric simulation for a bubble entrapment was performed with Froude number of 200 and Weber number of 138. Fig. 20 shows the numerical results for a bubble entrapment. After the drop impact on liquid pool, the cavity grows up in lower and outer direction. By the formation of cavity, the imbalance between the gravity and the surface tension were generated. As time elapses, the interface becomes stationary. Then, the impact velocity and gravity have an effect on the tendency of cavity collapse. Especially, the behavior of surface at the center of cavity determines the formation of bubble. In this case, the bubble was entrapped at the center of cavity.

## 6. CONCLUSIONS

A new level set formulation was developed for computing for simulation of various drop motions on orthogonal and non-orthogonal grids. An efficient formulation for contact angle modeling was incorporated into the level set method to account for the change between advancing and receding contact angles an immersed solid surface. The method was tested through the computations of droplet ejection and deposition in inkjet patterning process. From the numerical results, the method was proven to be applicable to investigate the effects of dynamic contact angle and pressure pulse type on the performance of an inkjet process and the multiphase characteristics between the liquid-gas solid phases can be used to overcome the patterning error. Furthermore the drop-drop and drop-pool collisions were numerically investigated. From the simulation of the binary drop collision, the behavior of drop and formation of satellite drop were successfully predicted. Also, the crown formation was predicted on the liquid film and bubble entrapment on liquid pool. These numerical results showed a good agreement with the theoretical and available experimental data.

## REFERENCES

[1] 1994, Sussman, M., Smereka, P. and Osher, S., “A Level Set Approach for Computing Solutions to Incompressible Two-Phase Flow,” *J. Comput. Phys.*, Vol.114, pp.146-159.

[2] 2004, Wu, H.C., Hwang, W.S. and Lin, H.J. “Development of a Three-Dimensional Simulation System for Micro-Inkjet and Its Experimental Verification,” *Mat. Sci. Eng. A*, Vol.220, pp.268-278.

[3] 2006. Yang, A.S. and Tsai, W.M., “Ejection Process Simulation for a Piezoelectric Microdroplet Generator,” *J. Fluid Eng.*, Vol.128, pp.1144-1152.

[4] 2005, Yu, J.D., Sakai, S. and Sethian, J., “A Coupled Quadrilateral Grid Level Set Projection Method Applied to Ink Jet Simulation,” *J. Compt. Phys.*, Vol.206, pp.227-251.

[5] 1985, Peric, M., *A Finite Volume Method for the Prediction of Three-Dimensional Fluid Flow in Complex Ducts*, Ph.D. thesis, University of London.

[6] 2006, Dong, H. and Carr, W.W., “An Experimental Study of Drop-on-Demand Drop Formation,” *Phys. Fluids*, Vol.18, p.072102.

[7] 2004, Yu, C., Lin, M., Hu, Y., Fu, T. and Chou, H., "Self-Alignment Optical Detection System for Droplet Based Biochemical Reactions," *Proceeding of IEEE Sensors 2004 Conference, Vienna, Austria*, pp.1206-1209.

[8] 1990, Ashgriz, N. and Poo, J., “Coalescence and Separation in Binary Collisions of Liquid Drops.” *J. Fluid Mech*., Vol.221, pp.183-204.

[9] 2005, Ko. G. and Ryou, H. “Modeling of Droplet Collision-induced Breakup Process.” *Int. J. Multiphase Flow*, Vol.31, pp.723-738.

[10] 2004, Cossali, G., Marengo, M., Coghe, A. and Zhdanov, S., “The role of time in single drop splash on thin film,” *Exp. Fluids*, Vol 36, pp.888-900.

[11] 1995, Yarin, A. and Weiss, D., “Impact of Drops on Solid Surfaces: Self-similar Capillary Waves, and Splashing as a New Type of Kinematic Discontinuity,” *J. Fluid Mech.*, Vol.283, pp.141-173.